

- observations of the 1996–1997 outburst of the microquasar GRO J1655–40. *Astrophys. J.* **520**, 776–787 (1999).
24. Merloni, A., Fabian, A. C. & Ross, R. R. On the interpretation of the multicolour disc model for black hole candidates. *Mon. Not. R. Astron. Soc.* **313**, 193–197 (2000).
25. Watarai, K., Fukue, J., Takeuchi, M. & Mineshige, S. Galactic black-hole candidates shining at the Eddington luminosity. *Publ. Astron. Soc. Jpn* **52**, 133–141 (2000).
26. Devillard, N. Eclipse users guide. (<http://www.eso.org/projects/aot/eclipse/eug/index.html>) (2000).
27. Phillips, S. N., Shahbaz, T. & Podsiadlowski, Ph. The outburst radial velocity curve of X-ray Nova Scorpii 1994 (=GRO J1655–40): a reduced mass for the black hole? *Mon. Not. R. Astron. Soc.* **304**, 839–844 (1999).
28. Fich, M., Blitz, L. & Stark, A. A. The rotation curve of the Milky Way to  $2 R_{\odot}$ . *Astrophys. J.* **342**, 272–284 (1989).
29. Warmels, R. H. in *Astronomical Data Analysis Software and Systems I* 115–119 (PASP Conf. Ser. 25, Astronomical Society of the Pacific, San Francisco, 1991).

# Acknowledgements

This work is based on observations collected at the European Southern Observatory, Chile.

Correspondence and requests for materials should be addressed to J.G.  
(e-mail: jgreiner@aip.de).

## Atomic structure holography using thermal neutrons

B. Sur\*, R. B. Rogge†, R. P. Hammond‡, V. N. P. Anghel\* & J. Katsaras†

\* Atomic Energy of Canada Limited, Chalk River Laboratories, Chalk River, Ontario K0J 1J0, Canada

† National Research Council, Steacie Institute for Molecular Sciences, Chalk River, Ontario K0J 1J0, Canada

‡ Department of Physics and Astronomy, McMaster University, Hamilton, Ontario L8S 4M1, Canada

The idea of atomic-resolution holography has its roots in the X-ray work of Bragg<sup>1</sup> and in Gabor's electron interference microscope<sup>2</sup>. Gabor's lensless microscope was not realized in his time, but over the past twelve years there has been a steady increase in the number of reports on atomic-resolution holography. All of this work involves the use of electrons<sup>3–6</sup> or hard X-rays<sup>7–11</sup> to produce the hologram. Neutrons are often unique among scattering probes in their interaction with materials: for example, the relative visibility of hydrogen and its isotopes is a great advantage in the study of polymers and biologically relevant materials. Recent work<sup>12</sup> proposed that atomic-resolution holography could be achieved with thermal neutrons. Here we use monochromatic thermal neutrons, adopting the inside-source concept of Szöke<sup>13</sup>, to image planes of oxygen atoms located above and below a single hydrogen atom in the oxide mineral simpsonite<sup>14</sup>.

The inside-source concept<sup>15</sup> uses the atoms making up the sample as independent sources of coherent illumination. In the case of X-ray holography and certain types of electron holography (such as auger holography), the radiation is generated by atomic de-excitation that propagates in the form of nearly spherical waves. This radiation can pass through the sample unperturbed (reference beam), or be scattered by the surrounding atoms (object beam). The interference between the reference and object beams produces the hologram. Similarly, incoherent scattering of thermal neutrons produces spherical waves. Hydrogen has a large incoherent neutron-scattering cross-section:  $\sigma_i = 80$  barns. Unlike forms of electromagnetic radiation that interact primarily with electrons, neutrons interact directly with nuclei and are, to first order, equally capable of imaging light atoms and heavy atoms. Consequently, atomic-resolution holographic images can be obtained of materials comprised entirely of light atoms (for example, hydrocarbons). Both

holography and conventional direct methods solve the phase problem in crystallography. Inside-source holography has the added advantage that only orientational order is required, that is, translational symmetry is not necessary. Holography is therefore also suitable for imaging non-crystalline materials such as nematic liquid crystals. Because of the large  $\sigma_i$  of hydrogen, thermal neutron holography should be particularly effective for the *ab initio* solution of organic macromolecule structures.

The sample used to demonstrate the feasibility of neutron holography was a single crystal of natural simpsonite, a rare oxide mineral of aluminium and tantalum with chemical formula  $\text{Al}_4\text{Ta}_3\text{O}_{13}(\text{OH})$ . Simpsonite was first discovered in western Australia<sup>14</sup> in 1939 and was examined using X-ray diffraction<sup>16</sup> the same year. More recently<sup>17</sup> X-ray diffraction has been used to refine the crystal structure in the trigonal space group *P3* with unit cell parameters  $a = 7.386(1) \text{ \AA}$  and  $c = 4.516(1) \text{ \AA}$ . Simpsonite contains only one H atom in the unit cell, which is convenient for this demonstration experiment.

We obtained our data at the N5 instrument located at the National Research Universal (NRU) reactor, Chalk River Laboratories, Canada. The experimental set-up is depicted in an annotated photograph in Fig. 1. Neutrons of wavelength  $\lambda = 1.3 \text{ \AA}$  with an estimated wavelength resolution of  $\Delta\lambda/\lambda \approx 1.5\%$  were obtained from a (113) reflection of a germanium monochromator. The sample-to-detector angular resolution was limited by distance collimation, as defined by a combination of an aperture in neutron-absorbing cadmium masks and the sample size, to approximately  $2^\circ$  vertically and  $2^\circ$  horizontally. The sample orientation ( $\phi$ ) and

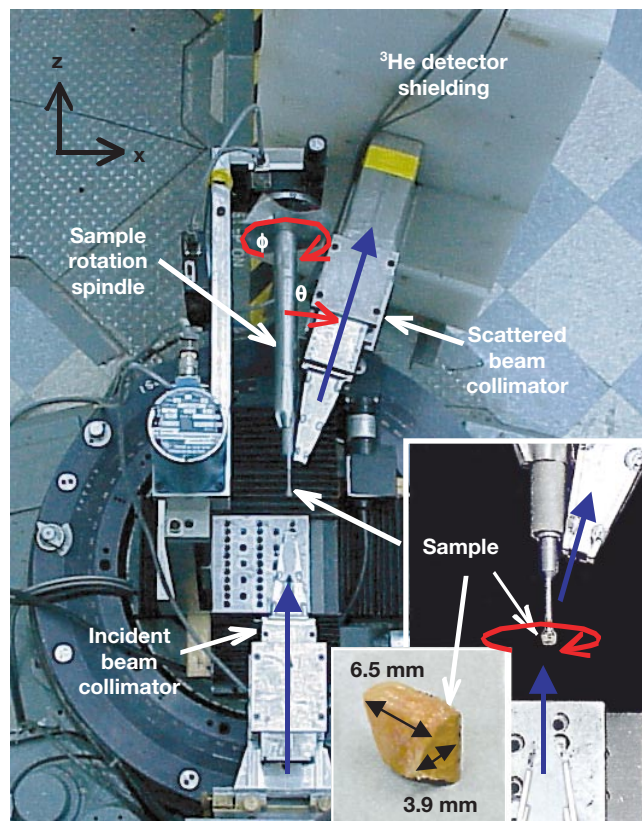


**Figure 1** Plan view photograph of the experimental set-up. The incident neutron beam (originating from the bottom of the photograph) is parallel to the sample rotation axis ( $\phi$ ). The hologram data was obtained by rotating the sample through  $2\pi$  radians, in optimal steps for the given detector coverage ( $2^\circ \times 2^\circ$ ), at a given detector angle  $\theta$ . This was repeated, in  $2^\circ$  steps in  $\theta$ , for  $17^\circ \leq \theta \leq 83^\circ$ . Interference between the scattered beam collimator and the sample rotation spindle imposed a lower limit on  $\theta$ .

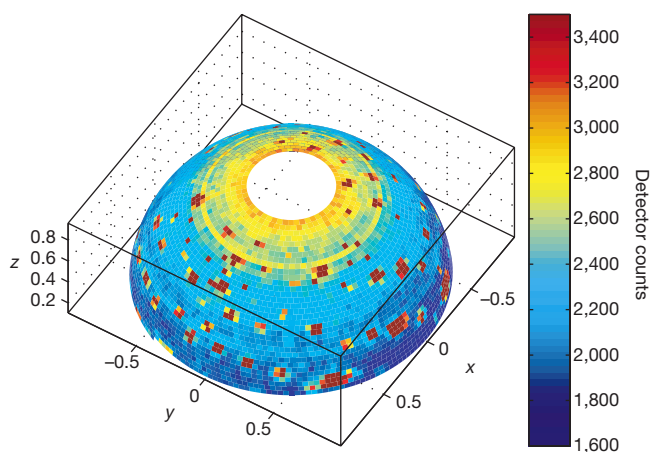


**Figure 2** Raw hologram data, plotted in  $2^\circ \times 2^\circ$  pixels on a surface of constant scattered wavevector magnitude ( $|\mathbf{k}_{\text{out}}| = 4.8 \text{ \AA}^{-1}$ ). Coordinates are oriented as indicated in Fig. 1, and labelled in units of  $k_{\text{out}}$ . Detector counts are indicated by colour. Bragg-spot intensities

are truncated at the largest colour value indicated. The thin yellow ring at about  $30^\circ$  from the pole is one of the aluminium lines.

detector angle ( $\theta$ ) were manipulated to optimally tile the scattered wavevector,  $\mathbf{k}_{\text{out}}$ , over most of a hemisphere of scattering from the sample. Data collection (total scattering and background) over approximately  $1.7\pi$  steradians in  $\mathbf{k}_{\text{out}}$  directions took 10 days of beam time to achieve sufficient statistical quality.

Figure 2 shows the raw intensity data, containing 4,334 solid-angle  $2^\circ \times 2^\circ$  pixels limited to  $17^\circ \leq \theta \leq 83^\circ$ . About 13% of the pixels contain evident, intense Bragg peaks that were judiciously excluded from the data analysis on a statistical basis. The remaining intensity data contains the hologram data plus a  $\theta$ -dependent background due to the vanadium pedestal and aluminium powder lines (at  $\theta = 32.3^\circ, 37.4^\circ, 54.0^\circ$  and  $64.3^\circ$ ) due to the aluminium wires used to secure the simpsonite crystal to the vanadium pedestal (Fig. 1). The measurements were repeated without the sample. This measured background, scaled by the measured sample transmission, was subtracted from the raw intensity data. The remaining scattered intensity distribution from the sample,  $I(\theta, \phi)$ , contains a  $\theta$ -dependent variation dominated by the H-atom incoherent elastic scattering Debye–Waller factor and an irregular variation in  $\theta$  and  $\phi$  of the self-attenuation owing to the highly asymmetric shape of the natural simpsonite sample (see smaller inset of Fig. 1). These variations were estimated by a least-squares fit of the background-subtracted intensity to slowly varying, phenomenological functions of the form  $D(\theta) = \alpha_1 \exp(\alpha_2(1 - \cos \theta))$  for the Debye–Waller factor, and  $S(\theta, \phi) = (\beta_0 + \beta_1\theta + \beta_2\theta^2 + \beta_3\theta^3)(\cos(\phi + \beta_4))$  for the effect of the irregular sample shape ( $\alpha_i, \beta_i$  are fitted parameters). The hologram modulation function is given by:

$$\chi(\theta, \phi) = \frac{I(\theta, \phi)}{D(\theta)S(\theta, \phi)} - 1 \quad (1)$$

From refs 12 and 18, the hologram modulation function for a scattering potential consisting of a strong incoherent scatterer at the origin, surrounded by a coherent scattering length distribution,  $b(\mathbf{r})$ , of pure s-wave, weak scatterers, is given by (aside from constants):

$$\chi(\mathbf{k}) \approx \int_{\text{all space}} \text{Re} \left( \frac{b(\mathbf{r})}{r} \exp(i(kr - \mathbf{k} \cdot \mathbf{r})) \right) d\mathbf{r} + O(b^2) \quad (2)$$

The conditions for pure s-wave, weak scattering are particularly well satisfied for unpolarized thermal neutron scattering from nuclei. Additionally, for most nuclei, the thermal neutron-scattering lengths are almost purely real and have the same sign<sup>19</sup>. As such, we can eliminate the conjugate image from a hologram made with a single thermal neutron wavelength. Thus, the real part of the

scattering potential can be directly reconstructed from the measured hologram modulation function using the following relations:

$$\tilde{b}_{\text{even}}(\mathbf{r}) = \frac{b(\mathbf{r}) + b(-\mathbf{r})}{kr} \cos(kr) \propto \int_{\text{constant } |\mathbf{k}|} \chi(\mathbf{k}) \cos(\mathbf{k} \cdot \mathbf{r}) d\mathbf{k} \quad (3)$$

$$\tilde{b}_{\text{odd}}(\mathbf{r}) = \frac{b(\mathbf{r}) + b(-\mathbf{r})}{kr} \sin(kr) \propto \int_{\text{constant } |\mathbf{k}|} \chi(\mathbf{k}) \sin(\mathbf{k} \cdot \mathbf{r}) d\mathbf{k} \quad (4)$$

For single-wavelength or constant- $|\mathbf{k}|$  data,  $b(\mathbf{r})$  cannot be directly determined by inversion of  $\tilde{b}_{\text{odd}}(\mathbf{r})$  and  $\tilde{b}_{\text{even}}(\mathbf{r})$ . However,  $\tilde{b}_{\text{odd}}(\mathbf{r}) \sin(kr)$  and  $\tilde{b}_{\text{even}}(\mathbf{r}) \cos(kr)$  can be combined by a moving average at the half-wavelength scale to give  $b(\mathbf{r})$ . Although this procedure permits the elimination of the conjugate image (that is,  $b(-\mathbf{r})$ ) in the reconstruction from single-wavelength data, one consequence is that the atomic positions are pushed outwards from the origin. This is because the neglected intensity of the imaginary part of the reconstructed wave is an exponential, decaying away from the origin. Combining holograms obtained at several different neutron wavelengths will eliminate such artefacts.

Following the above procedure, reconstructions from single-wavelength data are shown in Figs 3 and 4. The reconstructions for this demonstration experiment are not of the highest possible quality for the following reasons: (1) The data is incomplete along  $\theta$  and leads to a smearing out of the resolution along  $z$  of the reconstruction. (2) The counting statistics are just adequate—the statistical uncertainty per pixel is 2 to 3 per cent, whereas the expected hologram modulation, from theoretical considerations and simulations, is of the order of 0.5 per cent. This leads to a noisy reconstruction and limits the range over which the reconstruction is reliable. (3) The hologram reference beam is strongly modulated by the Debye–Waller factor of the source atom. (4) The shape correction does not fully account for the extremely asymmetric shape of the sample. The last two effects tend to produce asymmetric distortions of the real space reconstruction. Nonetheless, the data presented here demonstrate that the holographic *ab initio* reconstruction reproduces the known features of the simpsonite crystal structure (Figs 3 and 4).

The structure of simpsonite contains two layers of oxygen atoms perpendicular to the  $c$  axis of the crystal lattice. The first layer, which is closest to the hydrogen atom, has an oxygen atom located directly above (positive direction) the hydrogen atom along the direction of the  $c$  axis. This oxygen atom is surrounded by two triangular sublattices of oxygen atoms, slightly below the position of the central oxygen atom. In the second layer, located below (negative direction) the hydrogen atom, the oxygen atoms form triangular lattices about

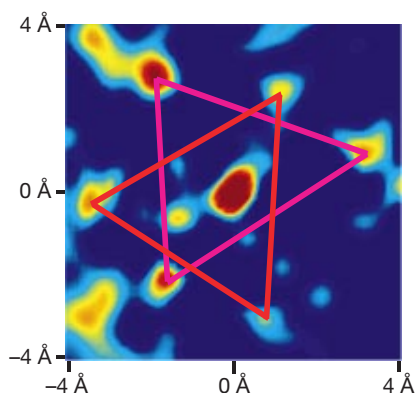


**Figure 3** Reconstructed plane located approximately  $+0.9 \text{ \AA}$  from the hydrogen atom (the origin). The plane is roughly coplanar to the basal plane of the crystal. The central spot is the oxygen atom located directly above the origin. The triangles are used to indicate the two triplets of oxygen atoms located slightly below this central oxygen atom. The distortion of the triangles is attributed to limitations in the quality of this demonstration data.

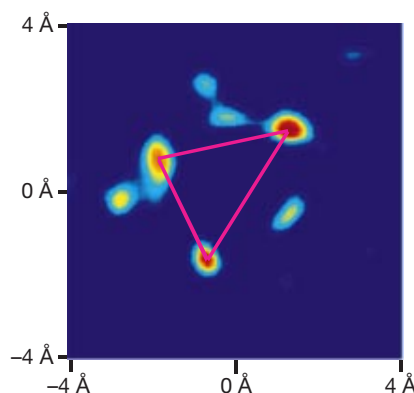
the perpendicular projection of the hydrogen atom onto this layer.

Figure 3 shows a reconstructed plane (approximately coplanar to the basal plane) at a distance of  $+0.9 \text{ \AA}$  from the incoherent source hydrogen atom (the origin of the reconstruction). There is a systematic distortion of the triangles (see overlays in Fig. 3) owing to the data quality limitations. Nevertheless, all of the expected oxygen atoms, the six of the two triangles and the central atom, are present in the reconstruction. From X-ray data<sup>17</sup> the oxygen–oxygen separation along the side of these triangles is around  $4.7 \text{ \AA}$ . On the basis of the reconstruction the average of the six oxygen–oxygen separations illustrated in Fig. 3 is around  $5.2 \text{ \AA}$  with a deviation from the mean of  $\pm 0.3 \text{ \AA}$ .

The next closest plane of oxygen atoms, found at a distance of  $-1.4 \text{ \AA}$  from the origin, is depicted in Fig. 4. From the reconstruction, it is easily seen that these oxygen atoms form a similarly distorted triangle of nearest neighbours whose average bond length is found to be  $3.1 \text{ \AA}$ , with a deviation from the mean  $\pm 0.5 \text{ \AA}$ . X-ray data<sup>17</sup> determine the oxygen bond lengths to be  $2.65 \text{ \AA}$ . The larger bond length deviation for this plane of oxygen atoms, as compared to those oxygen atoms found at  $0.9 \text{ \AA}$ , is attributed to a combination of poor vertical resolution and increased distance from the origin.

It should be noted that the distortion of the triangle in Fig. 4 is consistent with the observed distortion of the two triangles in Fig. 3. This systematic distortion provides confidence in the assertion that the observed distortions in the reconstruction are attributable to the effects already described. Consequently, it is expected that an accurate reconstruction can be realized with refinements to the data analysis, and with several data sets at various wavelengths, each approaching  $2\pi$  steradians in coverage, with improved resolution and statistical quality.

Thus we have shown for the first time, to our knowledge, that atomic-resolution holography can be achieved using thermal neutrons. The technique is based on using the incoherent scattering from atoms of the material as internal, isotropic neutron sources. Subsequent coherent scattering produces the hologram. For this data the very large incoherent scattering cross-section of the hydrogen atom was used to full advantage. This should make the technique of particular interest to studies of polymers and biological materials that are intrinsically rich in hydrogen. Also, because thermal neutrons are low in kinetic energy (of order meV) and carry no charge, they cause little or no damage in most materials, including delicate biological systems<sup>20,21</sup>. Spence<sup>22</sup> discusses in broad terms the implications and potential applications of the holography of atoms. The unique properties of neutrons—they distinguish atoms of similar  $Z$ , differentiate isotopes, couple to



**Figure 4** Reconstructed plane located approximately  $-1.4 \text{ \AA}$  from the hydrogen atom (the origin). The plane is roughly coplanar to the basal plane of the crystal. The centre of this triangle of nearest-neighbour oxygen atoms is located directly below the origin (defined by the hydrogen atom) in simpsonite. The distortion of the triangle is discussed in the text and the Fig. 3 caption.

magnetic moments, and to first-order coherently scatter equally well from light and heavy atoms—may now be used to address problems that cannot be solved by holography using electromagnetic radiation. In short, owing to the complementarity of neutrons with forms of electromagnetic radiation, thermal neutron atomic-structure holography is expected to become an essential tool for holographic techniques. □

Received 28 June; accepted 6 September 2001.

1. Bragg, W. L. The X-ray microscope. *Nature* **149**, 470 (1942).
2. Gabor, D. A new microscopic principle. *Nature* **161**, 777–778 (1948).
3. Harp, G. R., Saldin, D. K. & Tonner, B. P. Atomic-resolution electron holography in solids with localised sources. *Phys. Rev. Lett.* **65**, 1012–1015 (1990).
4. Zharnikov, M., Weinelt, M., Zebish, P., Stichler, M. & Steinrück, H.-P. First experimental determination of an adsorption site using multiple wave number photoelectron diffraction patterns. *Phys. Rev. Lett.* **73**, 3548–3551 (1994).
5. Sieger, M. T., Roesler, J. M., Lin, D.-S., Miller, T. & Chiang, T.-C. Holography of Ge(111)-(c(2×8) by surface core-level photoemission. *Phys. Rev. Lett.* **73**, 3117–3120 (1994).
6. Orchowski, A., Rau, W. D. & Lichte, H. Electron holography surmounts resolution limit of electron microscopy. *Phys. Rev. Lett.* **74**, 399–402 (1995).
7. Tegze, M. & Faigel, G. Atomic-resolution X-ray holography. *Europhys. Lett.* **16**, 41–46 (1991).
8. Gog, T. *et al.* Multiple-energy X-ray holography: atomic images of hematite ( $\text{Fe}_2\text{O}_3$ ). *Phys. Rev. Lett.* **76**, 3132–3135 (1996).
9. Tegze, M. & Faigel, G. X-ray holography with atomic resolution. *Nature* **380**, 49–51 (1991).
10. Tegze, M., Faigel, G., Marchesini, S., Belakhovsky, M. & Chumakov, A. I. Three dimensional imaging of atoms with isotropic  $0.5 \text{ \AA}$  resolution. *Phys. Rev. Lett.* **82**, 4847–4850 (1999).
11. Bompadre, S. G., Petersen, T. W. & Sorensen, L. B. Tabletop Bremsstrahlung X-ray holography: making multiwavelength X-ray holograms. *Phys. Rev. Lett.* **83**, 2741–2744 (1999).
12. Cser, L., Krexner, G. & Török, Gy. Atomic-resolution neutron holography. *Europhys. Lett.* **54**(6), 747–752 (2001).
13. Szöke, A. in *Short Wavelength Coherent Radiation: Generation and Applications*, Proc. Topical Meeting (eds Attwood, T. & Boker, J.) 361–467 (AIP Conf. Proc. No. 147, American Institute of Physics, New York, 1986).
14. Bowley, H. Simpsonite (sp. nov.) from Tabba Tabba, western Australia. *J. R. Soc. W. Aust.* **25**, 89–92 (1939).
15. Faigel, G. & Tegze, M. X-ray holography. *Rep. Prog. Phys.* **62**, 355–393 (1999).
16. Taylor, L. E. R. X-ray studies of Simpsonite. *J. R. Soc. W. Aust.* **25**, 93–97 (1939).
17. Ecri, T. S., Černý, P. & Hawthorne, F. C. The crystal chemistry of Simpsonite. *Can. Mineral.* **30**, 663–671 (1992).
18. Barton, J. J. Removing multiple scattering and twin images from holographic images. *Phys. Rev. Lett.* **67**, 3106–3109 (1991).
19. Sears, V. F. Neutron scattering lengths and cross sections. *Neutron News* **3**, 26–37 (1992).
20. Henderson, R. The potential and limitations of neutrons, electrons and X-rays for atomic-resolution microscopy of unstained biological molecules. *Q. Rev. Biophys.* **28**, 171–193 (1995).
21. Weik, M. *et al.* Specific chemical and structural damage to proteins produced by synchrotron radiation. *Proc. Natl Acad. Sci. USA* **97**, 623–628 (2000).
22. Spence, J. Holograms of atoms. *Nature* **410**, 1037–1040 (2001).

#### Acknowledgements

We acknowledge the intellectual contributions of I. P. Swainson and the expert technical assistance of J. H. Fox and L. E. McEwan. We also thank T. S. Ecri for providing the simpsonite crystal.

Correspondence and requests for materials should be addressed to R.B.R. (e-mail: ron.rogge@nrc.ca).